IEEE Access
Multidisciplinary | Rapid Review | Open Access Journal

Received February 18, 2021, accepted March 8, 2021, date of publication March 17, 2021, date of current version March 23, 2021.

*Digital Object Identifier 10.1109/ACCESS.2021.3066280*

# Displacement Sensor Integrated Into a Remote Center Compliance Device for a Robotic Assembly

**UIKYUM KIM[1], (Member, IEEE), DONG IL PARK[1], GWANGHYUN JO[2], HEEYEON JEONG[1], HWI-SU KIM[1], SUNG-HYUK SONG[1], AND CHANHUN PARK[1]**

[1]Department of Robotics and Mechatronics, Korea Institute of Machinery and Materials, Daejeon 34103, South Korea
[2]Department of Mathematics, Kunsan National University, Gunsan 54150, South Korea

Corresponding authors: Uikyum Kim (uikykim@gmail.com) and Chanhun Park (chpark@kimm.re.kr)

This work was supported in part by the Technology Innovation Program through the Ministry of Trade, Industry and Energy, Korean Government, under Grant 20012602, and in part by the Korea Institute of Machinery and Materials through the Basic Research Program under Grant NK233C.

**ABSTRACT** Compliance devices facilitate robotic assemblies by preventing excessive contact force on automated devices. However, the unavailability of displacement information regarding compliance devices makes it difficult to protect robots and objects during robotic assembly. It also limits repeatability and efficiency, especially regarding peg-in-hole and similar operations. We propose a six-axis displacement sensor installed on a remote center compliance device to detect the three translation and three rotation components generated by external forces and torques applied to the device, respectively. Triangular prism-shaped structures are used with capacitive sensing technology to measure the vertical and horizontal displacements in mm scale generated by the external normal and shear forces applied to the sensor. We designed and fabricated the sensor that could be integrated into a remote center compliance device, demonstrating it has a simple structure and is easy to install. To obtain six-axis force/torque information and six-axis displacement, calibration experiments were conducted using a specific setup and considering the device's geometry. The high sensing performance was verified through complementary experiments.

**INDEX TERMS** Six-axis displacement sensor, sensorized remote center compliance, six-axis force/torque sensor, capacitive sensor, compliance device.

## I. INTRODUCTION

Manipulators used for robotic assemblies require high performance in terms of their precision, repeatability, and speed, among other characteristics [1], [2]. For instance, slight misalignments may damage manipulators or peg-like objects through excessive contact forces during peg-in-hole assembly [1]–[4]. Compliant actuation can improve the effectiveness of robotic assemblies by protecting the robot and assembly objects from galling and jamming thus reducing contact forces. Remote center compliance (RCC) has been used to correct alignment errors and reduce contact forces during peg-in-hole and similar operations. In fact, the use of compliance devices has enabled robotic assemblies to operate without excessive contact forces during automated operation. Therefore, despite its low performance, a robot with RCC can conduct several important robotic assembly processes. However, a significant problem remains to be addressed before existing compliance devices can be improved. Although RCC devices allow passive motion to prevent excessive contact forces (according to their stiffness), the unavailability of displacement or force information during this passive motion limits their efficiency.

Six-axis force/torque (F/T) sensing is required to determine the displacement generated at a point in an RCC device. This sensing scheme provides three orthogonal force components ($F_x$, $F_y$, and $F_z$) and three orthogonal torque components ($T_x$, $T_y$, and $T_z$) at a point [5], [6]. The corresponding three translation components are $d_x$, $d_y$, and $d_z$, and the three rotation components are $\theta_x$, $\theta_y$, and $\theta_z$. This force and displacement information allows for the operation of an RCC device to be monitored, making it possible to compensate for any displacement errors during robotic assembly. Various studies have investigated six-axis F/T or displacement sensing for RCC devices. Although a six-axis F/T sensor using strain gauges and resistive sensing is commercially

The associate editor coordinating the review of this manuscript and approving it for publication was Xiaokang Yin.

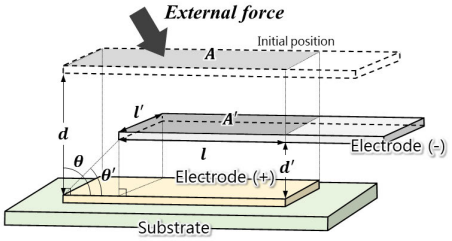


**FIGURE 1.** Sensing principle of a capacitive sensor composed of two parallel electrodes.

available [7], it is expensive given that it is difficult to fabricate and install [8]–[13]. It is also challenging to manually attach and wire the strain gauges to this sensor. In addition, it is demanding to combine this sensor with other devices because additional measuring devices such as an amplifier are required. Therefore, inexpensive sensors are needed for RCC devices, such as F/T sensors that use light and capacitance measurements and provide six-axis F/T sensing with a simple, easily assembled structure [6], [14]–[17]. Although these devices can be used for displacement sensing, they have not yet been devised as displacement sensors. Typical deformations requiring RCC are around 2 mm [18]; hence, a specific sensor is required that can measure six-axis F/T components and passive RCC deformation, and that can be easily installed on an RCC.

A capacitive two-axis force sensor has been developed that uses a triangular prism structure to measure vertical and horizontal forces [19]. However, it is difficult to measure the mm-scale displacements that occur in RCC with this sensor's technology. In addition, no technology has yet been proposed to extend this to a six-axis sensor, and to date no theoretical approach for measuring displacement has been suggested. In this study, we propose a novel six-axis displacement sensor that can be integrated into an RCC device, based on sensing technology. Through theoretical analysis of the relationship between displacement and capacitance, we designed triangular prism structures to measure the vertical and horizontal displacements generated by the external normal and shear forces applied to the sensor, thus obtaining a six-axis displacement sensor with six-axis F/T sensing ability and a simple structure. We verified this device's sensing ability by comparing it with a reference six-axis F/T sensor. Moreover, we analyzed the stiffness based on the geometric relation of the RCC to obtain the six-axis displacement information and experimentally evaluated the sensor's performance.

## II. SENSING PRINCIPLE

### A. ANALYSIS OF CAPACITANCE CHANGE CONSIDERING THE FRINGING EFFECT

Figure 1 illustrates a typical capacitive sensor composed of negative and positive electrodes on a substrate. The distance, $d$, and overlapping area, $A$, between the two electrodes are changed to $d'$ and $A'$, respectively, by an external force applied to the negative electrode. The resulting electrostatic capacitance variation of the sensor, $C_s$, is expressed as [20]

$$C_s = \varepsilon_0 \varepsilon_r \frac{A}{d} = \varepsilon_0 \varepsilon_r \left( \frac{l}{d} - cot\theta \right) l', \tag{1}$$

where $\varepsilon_0$ and $\varepsilon_r$ are the dielectric constant and static relative permittivity of the material sandwiched between the two electrodes, respectively; $l$ and $l'$ represent the length and width of the area, respectively; and $\theta$ is the angle between the plane of the positive electrode and a plane between the left edges of the negative and positive electrodes. Hence, the capacitance variation can be expressed by $d$ and $\theta$ to denote the positional relationship of the displacement between the two electrodes.

For a film-type sensor, the fringing effect is negligible owing to the extremely small $d$ compared to $l$ [14]. However, when measuring a large deformation $d$, as shown in Fig. 1, the fringing capacitance is considerable. In this instance, the electrostatic capacitance, which includes the fringing capacitance, is defined as [14]

$$C = C_{in} + C_{out} = \varepsilon_0 \varepsilon_r \left( \frac{K'(k_{in})}{K(k_{in})} + \frac{K'(k_{out})}{K(k_{out})} \right), \tag{2}$$

where $C_{in}$ and $C_{out}$ are the capacitances generated between the two electrodes and from the outer surface, respectively; $K(k)$ is the complete elliptic integral of the first kind [14]; and $k_{in}$ and $k_{out}$ represent moduli that include the structural information of the capacitance. They are expressed as function of $d$ and $\theta$ as follows:

$$k_{in} = \frac{1 + exp(-\pi cot\theta')}{\sqrt{\left(1 + exp\left(-\pi\left(\frac{l}{d'} + cot\theta'\right)\right)\right)\left(1 + exp\left(\pi\left(\frac{l}{d'} - cot\theta'\right)\right)\right)}} \tag{3}$$

where positional information, such as the angle, distance, and overlapping area between the two electrodes, is included. Here, $k_{out} = 1$ because the two electrodes are parallel. Therefore, (2) can be simplified as

$$C = C(k_{in}) = \varepsilon_0 \frac{K'(k_{in})}{K(k_{in})}. \tag{4}$$

The capacitance can be expressed from the computation of $K$, as follows:

$$C = -\frac{\varepsilon_0}{\pi}[ln\lambda + ln(1 + 2\lambda^4 + 15\lambda^8 + \ldots)], \tag{5}$$

where

$$\lambda = \frac{1 - \sqrt{k'_{in}}}{2(1 + \sqrt{k'_{in}})}. \tag{6}$$

Let $a = exp(\pi \ell / d)$ and $t = exp(-cot\theta)$. Then, (3) is expressed as

$$k_{in}^2 = \frac{(1+t)^2}{(1+ta)(1+t/a)}$$
$$(k'_{in})^2 = 1 - k_{in}^2 = \frac{(\sqrt{ta} + \sqrt{t/a})^2}{(1+ta)(1+t/a)}. \tag{7}$$

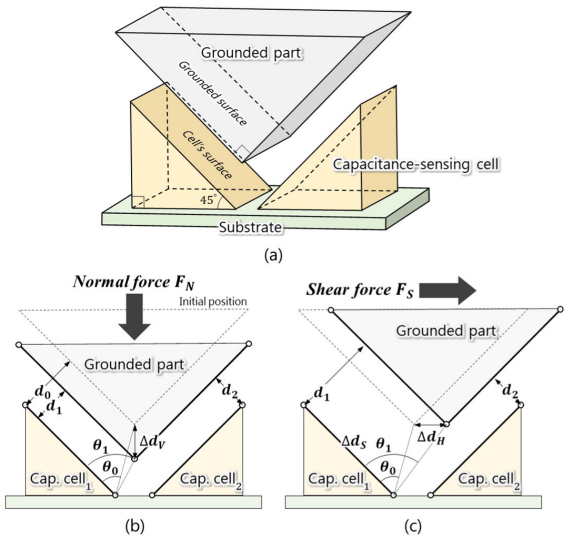


**FIGURE 2.** Sensing principle for detecting vertical and horizontal displacements: (a) sensor structure composed of three triangular prisms, (b) vertical displacement by normal force, and (c) horizontal displacement by shear force.

By neglecting $t/a$ and the high-degree terms $e^{-2c}, e^{-3c} \ldots$ we obtain

$$k'_{in} = \sqrt{\frac{exp(c)}{1+exp(c)}} = \sqrt{1-exp(-c)+exp(-2c)\ldots} = \sqrt{1-exp(-c)} \quad (8)$$

By the convergence of infinite geometric series, $\sum_i (ar^i) = a/(1-r)$, where $c = \pi\,(\ell/d - cot\theta)$. Now,

$$ln\lambda = ln\frac{1-\sqrt{k'_{in}}}{2(1+\sqrt{k'_{in}})} = ln(1-k'_{in}) - ln2 - 2ln(1+\sqrt{k'_{in}}) = -c - ln\left(2(1+\sqrt{1-e^{-c}})(1+\sqrt[4]{1-e^{-c}})^2\right). \quad (9)$$

The terms in (3) satisfy $exp(-\pi(\frac{l}{d} + cot\theta)) \gg 1 \gg exp(\pi(l/d - cot\theta))$, with the last expression having a negligible effect. Hence, $k'_{in}$ can be expressed as

$$k'_{in} = \sqrt{1-k_{in}^2} \approx \sqrt{1-exp\left(\pi\left(\frac{\ell}{d} - cot\theta\right)\right)}, \quad (10)$$

and the total capacitance is given by

$$C(d,\theta) = \varepsilon_0\left(\frac{\ell}{d} - cot\theta\right) + C_{fri} \quad (11)$$

where the fringing capacitance is expressed as

$$C_{fri} = \frac{\varepsilon_0}{\pi}\left[ln\left(2(1+\sqrt{1-e^{-c}})(1+\sqrt[4]{1-e^{-c}})^2\right) - ln(1+2\lambda^4+15\lambda^8+\ldots)\right]. \quad (12)$$

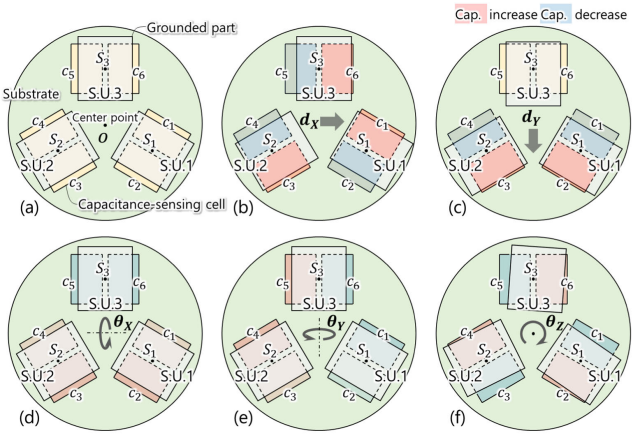


**FIGURE 3.** Geometric relationship between vertical/horizontal displacements and six-axis translation and rotation components at a sensing point on plane: (a) configuration of the sensor, (b) motion by $d_x$, (c) motion by $d_y$, (d) motion by $\theta_x$, (e) motion by $\theta_y$, and (f) motion by $\theta_z$.

**TABLE 1.** Capacitance changes of six capacitance cells related to six-axis displacement.

| Disp. \ c | 1 | 2 | 3 | 4 | 5 | 6 |
|---|---|---|---|---|---|---|
| $d_X$ | ↑ | ↓ | ↑ | ↓ | ↓ | ↑ |
| $d_Y$ | ↓ | ↑ | ↑ | ↓ | - | - |
| $d_Z$ | ↑ | ↑ | ↑ | ↑ | ↑ | ↑ |
| $\theta_X$ | ↑ | ↑ | ↑ | ↑ | ↓ | ↓ |
| $\theta_Y$ | ↓ | ↑ | ↑ | ↑ | ↑ | ↓ |
| $\theta_Z$ | ↓ | ↑ | ↓ | ↑ | ↓ | ↑ |

### B. VERTICAL/HORIZONTAL DISPLACEMENT SENSING

Six components are required to completely describe the six-axis displacement at a point, corresponding to three orthogonal translation components and three orthogonal rotation components (e.g., six-axis F/T sensor) [14]. Vertical/horizontal displacement sensing is thus required. Normal/shear force sensing using a triangular prism has previously been investigated to measure forces with equal sensitivity [19]. In this study, we used this principle of vertical/horizontal displacement sensing to obtain a simple sensor structure with a large displacement range. Fig. 2(a) illustrates a vertical/horizontal displacement sensor consisting of three triangular prisms on a substrate. The top prism is used as the grounded part and the two bottom prisms are used as capacitance sensing cells. In this configuration, two gaps are generated between the facing surfaces of the three prisms. Based on the aforementioned capacitance analysis, the capacitance variations $\Delta C_{V/H}$ of the vertical/horizontal displacements are given by

$$\Delta C_{V/H} = \Delta C_1(d_1,\theta_1) + \Delta C_2(d_2,\theta_2), \quad (13)$$

where $d_1$ and $d_2$ are the distances between surfaces, whereas $\theta_1$ and $\theta_2$ are the angles between the plane of the grounded part and the two cells, as shown in Fig. 2(b), in which $d_0$ and

$\theta_0$ are the initial values of the two cells. As the two distances change equally under a vertical displacement, each displacement and angle remain equal, with symmetric capacitance responses. Thus, the distance $d_{1/2}$ ($d_1$ and $d_2$) and angles $\theta_{1/2}$ ($\theta_1$ and $\theta_2$) can be calculated as

$$\begin{aligned} d_{1/2} &= d_0 + \Delta d_V cos45^\circ \\ \theta_{1/2} &= arccot\left(\frac{d_0 cot(\theta_0) - \Delta d_V cos45^\circ}{d_0 - \Delta d_V cos45^\circ}\right), \end{aligned} \tag{14}$$

However, the two distances differ with asymmetric capacitance responses under horizontal displacement, as shown in Fig. 2(c). The distance between the parallel plates changes as follows:

$$\begin{aligned} d'_{left} &= d + \Delta d_x cos45^\circ, \\ d'_{right} &= d - \Delta d_x cos45^\circ, \end{aligned} \tag{15}$$

for the left and right parts of the structure, respectively. $\Delta d_x$ is a displacement in the $x$-axis direction. The angle between the parallel plates changes as

$$\begin{aligned} \theta'_1 &= arccot\left(\frac{d_0 cot\theta_0 - \Delta d_s/\sqrt{2}}{d_0 cot\theta_0 + \Delta d_s/\sqrt{2}}\right), \\ \theta'_2 &= arccot\left(\frac{d_0 cot\theta_0 + \Delta d_s/\sqrt{2}}{d_0 cot\theta_0 - \Delta d_s/\sqrt{2}}\right). \end{aligned} \tag{16}$$

### C. GEOMETRIC RELATIONSHIP BETWEEN SIX-AXIS DISPLACEMENT AND VERTICAL/HORIZONTAL DISPLACEMENTS

The vertical/horizontal displacement sensor illustrated in Fig. 2 comprises a sensing unit. Three sensing units can be used to measure the three horizontal and three vertical displacements; these can be converted into a six-axis displacement measurement at the center of the substrate [14]. To this end, here three sensing units were arranged as $S_1$ to $S_3$ (Fig. 3(a)) on the substrate at 120-degree intervals; the six capacitance sensing cells ($c_1$ to $c_6$) in the three sensing units were arranged as shown in Fig. 3(a). The ground surfaces in the three units comprised a single grounded part for six-axis sensing. As shown in Fig. 3, the sensing units produced six different measurement combinations of cell measurement for six-axis displacement sensing at the center point. In this figure, red and blue colors indicate increasing and decreasing capacitances in the cell, respectively. When the grounded part moves along the $d_x$ direction, the capacitances at $c_1$, $c_3$, and $c_6$ increase and those at $c_2$, $c_4$, and $c_5$ decrease, as shown in Fig. 3(b). When the grounded part moves along the $d_y$ direction, the capacitances at $c_1$ and $c_4$ decrease and those at $c_2$ and $c_3$ increase, as shown in Fig. 3(c). The capacitances at $c_5$ and $c_6$ do not change because there is no change in the overlapping area between the two cells and the ground surface. Regarding movement along the $d_z$ direction, the capacitances at all cells increase. As shown in Figs. 3(d)–3(f), the sensing cells produce distinguishable capacitance patterns even when the grounded part moves around the three rotation axes. The capacitance changes of the six cells during six-axis displacement are summarized in Table 1, where "↑" and "↓" represent increases and decreases in capacitance, respectively, and "-" denotes no capacitance change.

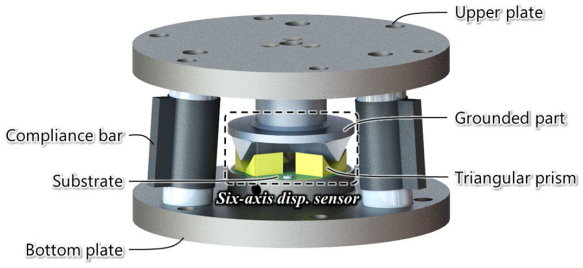


**FIGURE 4. Configuration of proposed six-axis displacement sensor installed on an RCC device.**

## III. SENSOR DESIGN AND FABRICATION

### A. DESIGN OF THE PROPOSED SENSOR INTEGRATED INTO AN RCC DEVICE

The sensor was designed with a focus on compactness, ease of manufacture, and ease in integrating it into an RCC, while also measuring the six-axis displacement. The developed six-axis displacement sensor is composed of a grounded part and the three sensing units, comprising six triangular prisms used as capacitance sensing cells on a substrate, as shown in Fig. 4. The triangular prisms are fixed to the substrate by bolted connections. To make the six gaps ($d_1$ to $d_6$) between the six triangular prisms and the grounded part, three triangular pillars are placed on the bottom of the grounded part. To integrate the six-axis displacement sensor to an RCC device consisting of three compliance bars, a top plate, and a bottom plate, the grounded part is suspended in the center of the upper part of the device. The compliance bar is deformed axially and laterally by external contact forces. The substrate, including the six triangular prisms, is placed at the center of the bottom plate. Therefore, the displacements generated by deformation of the three compliance bars move the top plate with the grounded part, while the bottom plate remains fixed. The corresponding motion is measured by the sensor. The resulting RCC device is compact, contains the sensor within its structure, and operates as a conventional RCC device while additionally providing six-axis displacement measurements.

### B. INTEGRATION OF THE PROPOSED SIX-AXIS DISPLACEMENT SENSOR INTO AN RCC DEVICE

Figure 5 shows the fabricated six-axis displacement sensor integrated into an RCC device, illustrating its simple installation. The sensor and RCC device have diameters of 32 mm and 80 mm, respectively. Figure 6 shows the three compliance bars (HCL-11A, ATI Industrial Automation, Apex, NC, USA) placed outside the bottom plate at intervals of 120° and assembled at 4 degrees between the top and bottom plates. Six rectangular electrodes of 5 × 8 $mm^2$ are placed on the front surface of the sensing PCB as a substrate. In addition, six triangular prisms (composed of aluminum alloy to provide

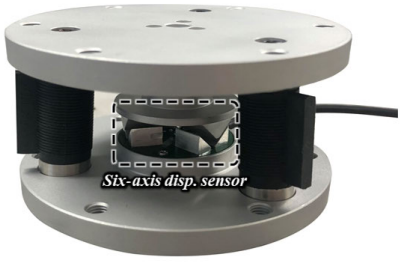


**FIGURE 5.** Manufactured six-axis displacement sensor integrated into an RCC device.

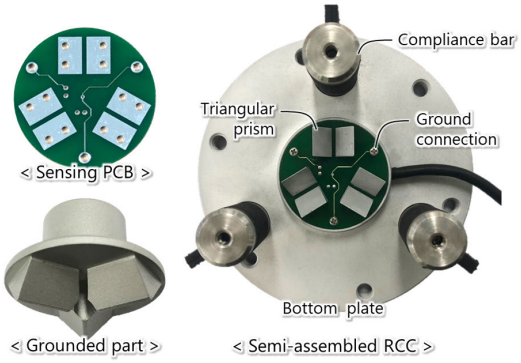


**FIGURE 6.** Sensing printed circuit board (PCB), grounded part of developed sensor, and partially assembled RCC with integrated sensor.

high electrical conductivity) act as capacitance sensing cells when connected to the rectangular electrodes by bolted connections, as shown in the right-hand side of Fig. 6. Each prism forms an isosceles right-angled triangle with base of 8 mm and height of 5 mm. The grounded part is designed to make six gaps of 2 mm between its surface and the surfaces of the six prisms. Therefore, the working range of the sensor is 2 mm. To connect the bottom plate, top plate, and grounded part to a common ground, a ground pad is fixed to the bottom plate by a bolted connection, as shown in the right-hand side of Fig. 6. Thus, passive shielding minimizes noise from outer electromagnetic interference [23]. As the capacitive sensor is very sensitive to changes in external electromagnetic interference, the sensing PCB includes a capacitance-to-digital converter (CDC) chip to directly output digital signals. A CDC chip (AD7147, Analog Devices, Norwood, MA, USA) is installed on the bottom surface to measure the six capacitances generated between the six prisms and the grounded part. The digitalized capacitance data are transferred by an $I^2C$ communication interface to a microcontroller unit. The four wires from the sensor are dedicated to the interface and power source (5 V) of the sensor.

## IV. EXPERIMENTAL EVALUATION

Calibration is necessary to obtain six-axis displacement measurements from the developed sensor. For calibration, reference displacement measurements should be collected from the sensor along with capacitance measurements. However, no reference sensor is available for six-axis

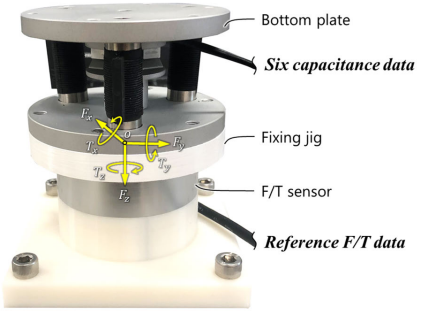


**FIGURE 7.** Experimental setup for F/T calibration and verification of sensing performance.

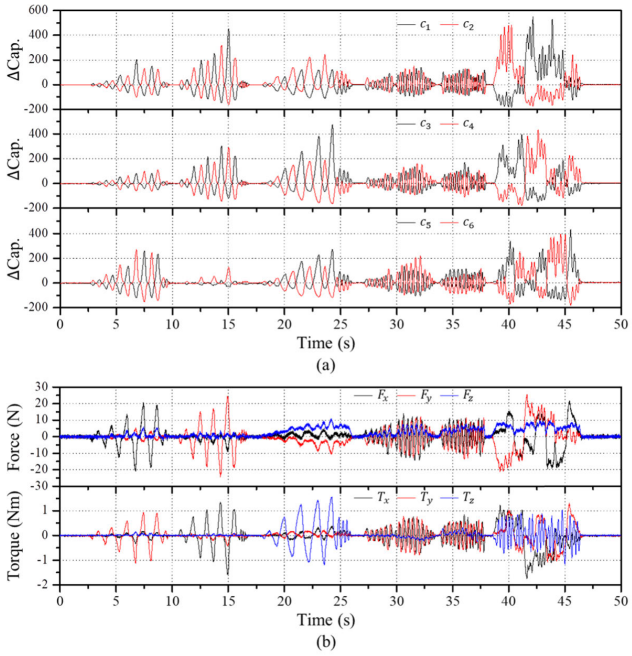


**FIGURE 8.** Experimental data for calibration: (a) six capacitance values measured by the developed sensor. (b) Reference six-axis F/T measurements.

displacement measurements in RCC devices. Therefore, reference data for calibration should be obtained from six-degrees-of-freedom automated stages or Stewart platforms that form at least a hexapod positioner. However, commercial stages and hexapods are very expensive and have limited uses. Therefore, here we designed a calibration process comprising two steps. First, we calibrated the six capacitance values to six-axis F/T values. This step was easy to perform because a reference sensor can be used to measure the six-axis F/T information. During this step, uncertainties such as machining errors were considered during calibration, as they were reflected in the F/T information. Second, we calibrated the F/T information as six-axis displacement measurements using the relationship between displacement and force. We conducted this two-step displacement calibration and analyzed the experimental results. Therefore, the relationship between the capacitance values and the displacement can be

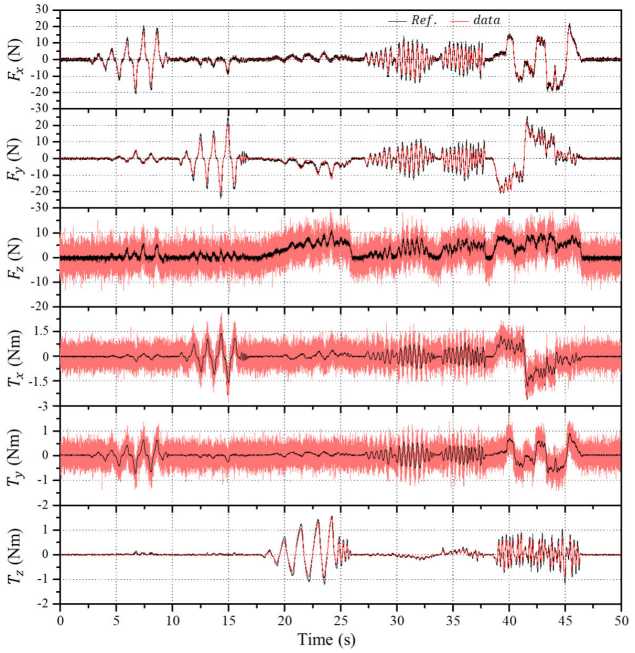


**FIGURE 9.** Time-domain responses of six-axis F/T measurements from the developed sensor (red) and a reference sensor (black).

summarized as

$$\mathbf{K}^{-1} \cdot \mathbf{A} \cdot [c_1^{-1}\ c_2^{-1}\ c_3^{-1}\ c_4^{-1}\ c_5^{-1}\ c_6^{-1}]^T = [d_x\ d_y\ d_z\ \theta_x\ \theta_y\ \theta_z]^T, \quad (17)$$

where $\mathbf{K}$ is a stiffness matrix representing the relationship between the F/T and the displacement. $\mathbf{A}$ is a calibration matrix representing the relationship between the capacitance values and the F/T. A detailed explanation is presented in the following subsections.

### A. CALIBRATION AND EVALUATION OF SIX-AXIS F/T MEASUREMENTS

To proceed with the six-axis F/T calibration, we established an experimental setup to match the sensing points of the developed sensor and those of the reference sensor, such that both experienced the same forces and torques, as shown in Fig. 7. The setup consisted of one reference sensor (RFT60-HA01 F/T sensor, Robotous, Seongnam-si, Korea) and two jigs. The relationship between the capacitance measurements from the sensor and the six-axis F/T measurements from the reference is expressed as

$$\mathbf{A} \cdot [c_1^{-1}\ c_2^{-1}\ c_3^{-1}\ c_4^{-1}\ c_5^{-1}\ c_6^{-1}]^T = [F_x\ F_y\ F_z\ T_x\ T_y\ T_z]^T, \quad (18)$$

where $\mathbf{A} \in \mathbf{R}^{6\times6}$ is the calibration matrix, $[c_1^{-1}\ c_2^{-1}\ c_3^{-1}\ c_4^{-1}\ c_5^{-1}\ c_6^{-1}]^T$ is the vector of reciprocals of the six capacitances measured by the developed sensor, and $[F_x\ F_y\ F_z\ T_x\ T_y\ T_z]^T$ is the vector of the six-axis F/T measurements obtained from the reference. The calibration method for the F/T measurement has been outlined in previous studies [6], [14], [21]. Capacitance has a nonlinear relationship with force. Therefore, each

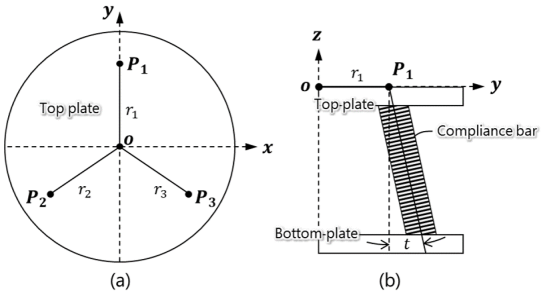


**FIGURE 10.** Geometric relationship of forces and displacements between the compliance bar and the RCC.

capacitance value was made into a function, and the linear least-square method was used to automatically calculate and obtain the component of the matrix that could minimize the error between the data of the two sensors. We used capacitance reciprocals because the theoretical relationship between force and capacitance is not linear. It is therefore appropriate to express it as the fractional function in (18). Figure 8 illustrates the six capacitance values measured by the developed sensor simultaneously with the F/T measured by the reference sensor when applying six-axis F/T to the RCC device. Using (18) with these experimental data, we obtained the following matrix $\mathbf{A}$:

$$\mathbf{A} = \begin{bmatrix} 30.5 & 25.6 & -7.41 & 9.75 & -29.2 & -32.1 \\ -10.9 & -15.3 & 34.5 & 23.4 & -27.7 & -0.45 \\ 30.3 & 14.1 & 19.6 & 24.7 & 26.1 & 37.4 \\ 0.99 & 1.52 & -1.45 & -0.75 & 2.28 & 0.52 \\ 1.55 & 1.31 & -0.46 & 0.49 & -1.78 & -1.81 \\ 1.37 & -1.08 & 1.71 & -1.86 & 0.92 & -1.44 \end{bmatrix} \times 10^6. \quad (19)$$

The six measured capacitances were converted into F/T using matrix $\mathbf{A}$. As shown in Fig. 9, the F/T measured using the developed sensor agreed with the reference F/T data in the time domain, obtaining mean relative errors for the three force components of 0.41, 0.51, and 33.7% of the full-scale force/torque ranges, and for the three torque components of 27.3, 21.8, and 0.21%. The obtained resolutions were 13 mN, 26 mN, and 5.2 N for the three forces, and 0.61 Nm, 0.57 Nm, and 1.2 mNm for the three torques. Owing to the characteristics of the compliance bar used in the RCC device, the axial stiffness of the bar was much higher than its lateral stiffness [18], and consequently the deformation was small when $F_z$, $T_x$, and $T_y$ were applied. This explains the relatively low resolutions of these components.

### B. RELATIONSHIP BETWEEN SIX-AXIS DISPLACEMENT AND F/T

As mentioned earlier, six-axis displacement is related to the measured F/T as follows. For each spring, one end is fixed to the top plate and the other was fixed to the bottom plate. For convenience, we assume that the top plate is perpendicular to

the $z$-axis and its center is located at origin $O$. One of the ends of each of the springs $s_1$, $s_2$, and $s_3$ are respectively fixed at

$$P_1(0, r_0, 0), \quad P_2(-r_0\cos(\pi/6), \quad -r_0\sin(\pi/6)r_0, 0),$$
$$P_3(r_0\cos(\pi/6), \quad -r_0\sin(\pi/6)r_0, 0).$$

We define $\mathbf{r}_1 = \overrightarrow{OP_1}$, $\mathbf{r}_2 = \overrightarrow{OP_2}$, and $\mathbf{r}_3 = \overrightarrow{OP_3}$.

The bottom plate is located below the structure at a distance $h$ from the top plate. Each spring is nearly parallel to the $z$-axis, but is slightly tilted outward at an angle of $t$, as shown in Fig. 10. By considering the spring geometry, the unit normal vector $\mathbf{n}_i$ $(i = 1, 2, 3)$ of spring $s_i$ is given by

$$\mathbf{n}_1 = (0, -\sin t, \cos t), \quad \mathbf{n}_2 = (\frac{\sqrt{3}}{2}\sin t, \frac{1}{2}\sin t, \cos t)$$
$$\mathbf{n}_3 = (-\frac{\sqrt{3}}{2}\sin t, \frac{1}{2}\sin t, \cos t).$$

The three springs have the same spring coefficients in the normal and shear directions.

Let us consider the decomposition of the force per spring $s_i$ $(i = 1, 2, 3)$. Suppose that $P_i$ varies with $\mathbf{d}$. Displacement $\mathbf{d}$ can be decomposed into the normal $(\mathbf{d_n})$ and shear $(\mathbf{d_s})$ directions of spring $s_i$ as follows:

$$\mathbf{d} = \mathbf{d}_{\mathbf{n}_i} + \mathbf{d}_{\mathbf{s}_i} = (\mathbf{d}\cdot\mathbf{n}_{s_i})\mathbf{n}_{s_i} + \mathbf{d} - (\mathbf{d}\cdot\mathbf{n}_{s_i})\mathbf{n}_{s_i}. \quad (20)$$

The resulting force of spring $s_i$ is given by

$$\mathbf{F}_i = -k_n\mathbf{d}_{\mathbf{n}_i} - k_s\mathbf{d}_{\mathbf{s}_i}. \quad (21)$$

### 1) EFFECT OF TRANSLATION

Let $\mathbf{x} = (x, 0, 0)$, $\mathbf{y} = (0, y, 0)$, and $\mathbf{z} = (0, 0, z)$. Here, we calculate the resulting forces $\mathbf{F}_1$, $\mathbf{F}_2$, and $\mathbf{F}_3$ exerted on springs $s_1$, $s_2$, and $s_3$ respectively due to translation. The resulting forces under translations $\mathbf{x}$, $\mathbf{y}$, and $\mathbf{z}$ are respectively denoted as $\mathbf{F}_1|_\mathbf{x}$, $\mathbf{F}_1|_\mathbf{y}$, and $\mathbf{F}_1|_\mathbf{z}$ is obtained by decomposing each translation with respect to the normal and shear directions of spring $s_1$ (20) and by the spring force formulation (21):

$$\mathbf{F}_1|_\mathbf{x} = [-k_s(1, 0, 0)]x,$$
$$\mathbf{F}_1|_\mathbf{y} = [-k_n(0, \rho, -\frac{1}{2}\sigma) - k_s(0, 1-\rho, \frac{1}{2}\sigma)]y,$$
$$\mathbf{F}_1|_\mathbf{z} = [-k_n(0, -\frac{1}{2}\sigma, 1-\rho) - k_s(0, \frac{1}{2}\sigma, \rho)]z, \quad (22)$$

with coefficients $\rho = \sin^2 t$ and $\sigma = \sin 2t$. Analogously, the resulting forces under translations $\mathbf{x}$, $\mathbf{y}$, and $\mathbf{z}$ for springs $s_2$ and $s_3$ are computed as

$$\mathbf{F}_2|_\mathbf{x} = [-\frac{\sqrt{3}k_n}{4}(\sqrt{3}\rho, \rho, \sigma) + k_s(\frac{3}{4}\rho - 1, \frac{\sqrt{3}}{4}\rho, \frac{\sqrt{3}}{4}\sigma)]x,$$
$$\mathbf{F}_2|_\mathbf{y} = [-\frac{k_n}{4}(\sqrt{3}\rho, \rho, \sigma) - k_s(-\frac{\sqrt{3}}{4}\rho, 1-\frac{1}{4}\rho, -\frac{1}{4}\sigma)]y,$$
$$\mathbf{F}_2|_\mathbf{z} = [-k_n(\frac{\sqrt{3}}{4}\sigma, \frac{1}{4}\sigma, 1-\rho) - k_s(-\frac{\sqrt{3}}{4}\sigma, -\frac{1}{4}\sigma, \rho)]z,$$
$$\mathbf{F}_3|_\mathbf{x} = [\frac{\sqrt{3}k_n}{4}(-\sqrt{3}\rho, \rho, \sigma) - k_s(1-\frac{3}{4}\rho, \frac{\sqrt{3}}{4}\rho, \frac{\sqrt{3}}{4}\sigma)]x,$$

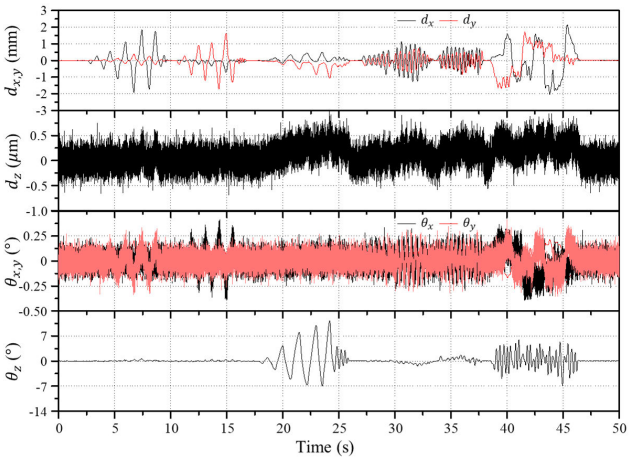


**FIGURE 11.** Time-domain response of six-axis displacement measured by the developed sensor.

$$\mathbf{F}_3|_\mathbf{y} = [-\frac{k_n}{4}(-\sqrt{3}\rho, \rho, \sigma) - k_s(\frac{\sqrt{3}}{4}\rho, 1-\frac{1}{4}\rho, -\frac{1}{4}\sigma)]y,$$
$$\mathbf{F}_3|_\mathbf{z} = [k_n(\frac{\sqrt{3}}{4}\sigma, -\frac{1}{4}\sigma, \rho-1) - k_s(\frac{\sqrt{3}}{4}\sigma, -\frac{1}{4}\sigma, \rho)]z. \quad (23)$$

By combining (22) and (23), we can obtain the force $\mathbf{F}$ exerted on the sensor by translations $\mathbf{x}$, $\mathbf{y}$, and $\mathbf{z}$:

$$\mathbf{F}|_\mathbf{x} = \sum_{i=1}^{3}\mathbf{F}_i|_\mathbf{x} = [-k_n(\frac{3}{2}\rho, 0, 0) - k_s(3-\frac{3}{2}\rho, 0, 0))]x,$$
$$\mathbf{F}|_\mathbf{y} = \sum_{i=1}^{3}\mathbf{F}_i|_\mathbf{y} = [-k_n(0, \frac{3}{2}\rho, 0) - k_s(0, 3-\frac{3}{2}\rho, 0)]y,$$
$$\mathbf{F}|_\mathbf{z} = \sum_{i=1}^{3}\mathbf{F}_i|_\mathbf{z} = [-k_n(0, 0, 3-3\rho) - k_s(0, 0, 3\rho)]z. \quad (24)$$

Now we compute the torques $\mathbf{T}_1$, $\mathbf{T}_2$, and $\mathbf{T}_3$ applied to springs $s_1$, $s_2$, and $s_3$, respectively, under translations $\mathbf{x}$, $\mathbf{y}$, and $\mathbf{z}$. By the definition of torque, for $\alpha = \mathbf{x}, \mathbf{y}, \mathbf{z}$, we have

$$\mathbf{T}_i|_\alpha = \mathbf{r}_i \times \mathbf{F}_i|_\alpha, \quad \mathbf{T}|_\alpha = \sum_{i=1}^{3}\mathbf{T}_i|_\alpha = \sum_{i=1}^{3}\mathbf{r}_i \times \mathbf{F}_i|_\alpha. \quad (25)$$

By substituting (22) and (23) into the expression above, we obtain $(\eta = k_n - k_s)$

$$\mathbf{T}|_\mathbf{x} = r_0(0, -\frac{3}{4}\eta\sigma, 0)x, \quad \mathbf{T}|_\mathbf{y} = r_0(\frac{3}{4}\eta\sigma, 0, 0)y,$$
$$\mathbf{T}|_\mathbf{z} = (0, 0, 0). \quad (26)$$

### 2) EFFECT OF ROTATION

Let us consider the rotation $\theta_z$ of the top plate about the $z$-axis. The locations of $P_1$, $P_2$, and $P_3$ change as follows:

$$P_1' = r_0(-\sin(\frac{\pi}{2} + \theta_z), \cos(\frac{\pi}{2} + \theta_z), 0),$$
$$P_2' = r_0(-\sin(\frac{7\pi}{6} + \theta_z), \cos(\frac{7\pi}{6} + \theta_z), 0),$$

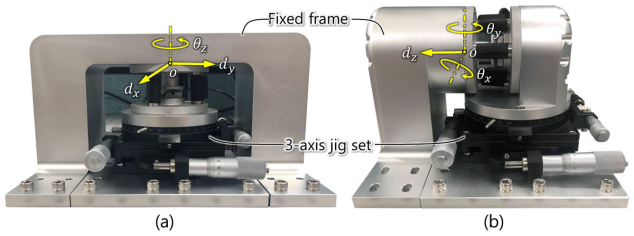


**FIGURE 12.** Experimental setups for evaluating displacement sensing in the developed RCC device: (a) two translations ($d_x$ and $d_y$) and one rotation ($\theta_z$), and (b) one translation ($d_z$) and two rotations ($\theta_x$ and $\theta_y$).

$$P_3' = r_0(-\sin(\frac{11\pi}{6}+\theta_z), \cos(\frac{11\pi}{6}+\theta_z), 0).$$

Assuming that $\theta_z$ is small, we obtain

$$\Delta P_1|_{\theta_z} := P_1' - P_1 \approx r_0(-\theta_z, 0, 0),$$
$$\Delta P_2|_{\theta_z} := P_2' - P_2 \approx r_0(\frac{1}{2}\theta_z, -\frac{\sqrt{3}}{2}\theta_z, 0),$$
$$\Delta P_3|_{\theta_z} := P_3' - P_3 \approx r_0(\frac{1}{2}\theta_z, \frac{\sqrt{3}}{2}\theta_z, 0),$$

and we can compute the force applied to springs $s_1$, $s_2$, and $s_3$:

$$\mathbf{F}_1|_{\theta_z} = \mathbf{F}_1|_{\Delta P_1|_{\theta_z}} = \mathbf{F}_1|_{(-r_0\theta_z,0,0)},$$
$$\mathbf{F}_2|_{\theta_z} = \mathbf{F}_2|_{\Delta P_2|_{\theta_z}} = \mathbf{F}_2|_{(\frac{1}{2}r_0\theta_z,0,0)} + \mathbf{F}_2|_{(0,-\frac{\sqrt{3}}{2}r_0\theta_z,0)},$$
$$\mathbf{F}_3|_{\theta_z} = \mathbf{F}_3|_{\Delta P_3|_{\theta_z}} = \mathbf{F}_3|_{(\frac{1}{2}r_0\theta_z,0,0)} + \mathbf{F}_3|_{(0,\frac{\sqrt{3}}{2}r_0\theta_z,0)}.$$

By substituting the above for the formula of force against displacement change, (22) and (23), we have

$$\mathbf{F}_1|_{\theta_z} = r_0(k_s, 0, 0)\theta_z, \quad \mathbf{F}_2|_{\theta_z} = r_0\left(-\tfrac{1}{2}k_s, \tfrac{\sqrt{3}}{2}k_s, 0\right)\theta_z,$$
$$\mathbf{F}_3|_{\theta_z} = r_0\left(-\tfrac{1}{2}k_s, -\tfrac{\sqrt{3}}{2}k_s, 0\right)\theta_z, \tag{27}$$

and we obtain the force $\mathbf{F}$ applied to the sensor under a small degree of rotation $\theta_z$:

$$\mathbf{F}|_{\theta_z} = \mathbf{F}_1|_{\theta_z} + \mathbf{F}_2|_{\theta_z} + \mathbf{F}_3|_{\theta_z} = (0, 0, 0). \tag{28}$$

To compute the torque under rotation $\theta_z$, we first consider the following expression:

$$\mathbf{T}_i|_{\theta_z} = \mathbf{r}_i \times \mathbf{F}_i|_{\theta_z}, \quad \mathbf{T}|_{\theta_z} = \textstyle\sum_{i=1}^{3} \mathbf{T}_i|_{\theta_z}.$$

By substituting $\mathbf{F}_i|_{\theta_z}$ in (27) into the above equations, we obtain

$$\mathbf{T}|_{\theta_z} = r_0^2(0, 0, -3k_s)\theta_z. \tag{29}$$

The effect of rotation $\theta_x$ ($\theta_y$) along the $x$-axis ($y$-axis) can be computed analogously:

$$\mathbf{F}|_{\theta_x} = r_0(0, \frac{3}{4}\eta\sigma, 0)\theta_x, \quad \mathbf{F}|_{\theta_y} = r_0(-\frac{3}{4}\eta\rho, 0, 0)\theta_y,$$
$$\mathbf{T}|_{\theta_x} = r_0^2(-\frac{3}{2}\eta(1-\rho) - \frac{3}{2}k_s, 0, 0)\theta_x,$$
$$\mathbf{T}|_{\theta_y} = r_0^2(0, -\frac{3}{2}\eta(1-\rho) - \frac{3}{2}k_s, 0)\theta_y. \tag{30}$$

#### 3) STIFFNESS MATRIX BETWEEN F/T AND DISPLACEMENT

First, we summarize the resulting force $\mathbf{F} = (F_x, F_y, F_z)$ and torque $\mathbf{T} = (T_x, T_y, T_z)$ under translation $(x, y, z)$ and rotation $(\theta_x, \theta_y, \theta_z)$. By (24), (26), (28), (29), and (30), we conclude that

$$\begin{bmatrix} F_x \\ F_y \\ F_z \\ T_x \\ T_y \\ T_z \end{bmatrix} = \begin{bmatrix} a & 0 & 0 & 0 & -c & 0 \\ 0 & a & 0 & c & 0 & 0 \\ 0 & 0 & b & 0 & 0 & 0 \\ 0 & c & 0 & e & 0 & 0 \\ -c & 0 & 0 & 0 & e & 0 \\ 0 & 0 & 0 & 0 & 0 & d \end{bmatrix} \cdot \begin{bmatrix} d_x \\ d_y \\ d_z \\ \theta_x \\ \theta_y \\ \theta_z \end{bmatrix}, \tag{31}$$

where $a = -\frac{3}{2}\eta\rho - 3\ k_s$, $b = 3\eta\rho - 3k_n$, $c = \frac{3}{4}r_0\eta\sigma$, $d = -3r_0^2k_s$, and $e = -(3r_0^2(-\rho\eta + k_n))/2$. Now, we can derive the designated transfer function. The $6 \times 6$ matrix is the inverse of $\mathbf{K}$. We provide $A$ for constants $r_0 = 0.027\ m$, $k_n = 4.444 \cdot 10^6\ N/m$, $k_s = 3.5 \cdot 10^3\ N/m$, $t = 4°$. Therefore, matrix $\mathbf{K}$ is defined as

$$\mathbf{K} = \begin{bmatrix} 9.5 & 0 & 0 & 0 & -24.6 & 0 \\ 0 & 9.5 & 0 & 24.6 & 0 & 0 \\ 0 & 0 & 7.5 \cdot 10^{-3} & 0 & 0 & 0 \\ 0 & -24.9 & 0 & -84.3 & 0 & 0 \\ 24.9 & 0 & 0 & 0 & -84.3 & 0 \\ 0 & 0 & 0 & 0 & 0 & 1.3 \cdot 10^4 \end{bmatrix} \times 10^{-5}. \tag{32}$$

The measured F/T displayed in Fig. 9 can be converted into the six-axis displacement using the calculated stiffness matrix, $\mathbf{K}$. Figure 11 shows the three-axis translation and the three-axis rotation. As the maximum displacements of the robot effector are 2 mm and 10 degrees, we expect that these values were correctly measured. We verified the sensor resolutions to be 1.2 $\mu$m, 2.3 $\mu$m, and 0.47 mm for the three translation components, and 0.14, 0.11, and 0.008 degrees for the three rotation components. The accurate force measurement should provide a high-accuracy displacement measurement. However, we conducted experiments with additional experimental setups to further evaluate the sensor accuracy.

### C. EVALUATION OF SIX-AXIS DISPLACEMENT MEASUREMENTS

As mentioned earlier, the performances of displacement measurements can be verified using a six-degree-of-freedom mechanism device such as a Stewart platform. However, these devices are expensive and difficult to obtain with suitable displacement and sensitivity. Figure 12 shows the two experimental setups that we adopted to evaluate the displacement sensing performance of the developed sensor. As shown in Fig. 12(a), the top surface of the RCC device is fixed to an aluminum alloy frame, and the bottom surface is fixed to a three-axis jig set comprising two manual linear stages (XYSPG100, MISUMI, Tokyo, Japan) and one rotational stage (RPGT100, MISUMI). Hence, this setup applies two

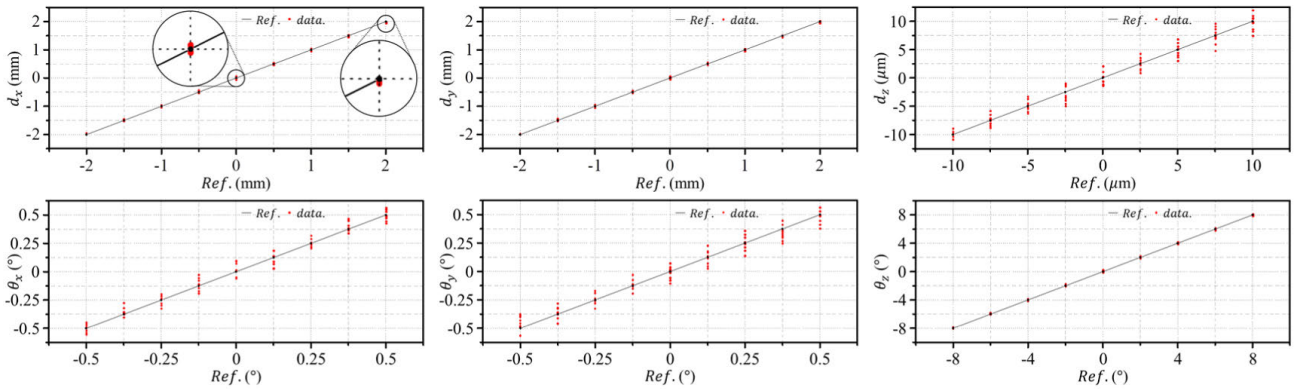


**FIGURE 13.** Experimental results of measured displacement values with reference data.

translations ($d_x$ and $d_y$) and one rotation ($\theta_z$) in this case. Moreover, as shown in Fig. 12(b), the setup can apply one translation ($d_z$) and two rotations ($\theta_x$ and $\theta_y$). We evaluated the performances of the six-axis displacement measurements using these displacements. Figure 13 shows the displacement measurements obtained from the developed sensor, where the values correspond to multiplying the capacitance by (19) and (32). Each translation $d_x$ and $d_y$ was measured ten times in $\pm 2$ mm sections at 0.5 mm intervals, and the rotation $\theta_z$ was measured in a $\pm 8°$ section at 2° intervals. In addition, $d_z$ was measured in a $\pm 10$ $\mu$m section at 2.5 $\mu$m intervals, and $\theta_x$ and $\theta_y$ were measured in $\pm 0.5°$ sections at 0.125° intervals. The mean error of displacement was the highest at the largest displacement, reaching 0.9, 1.2, 39.7, 31.7, 29.8, and 0.47% of the full-scale displacement ranges. Moreover, the mean value of the highest repeatability, 0.89%, was achieved at the maximum displacement. Furthermore, the mean value of the lowest repeatability, 2.7%, was obtained at the zero point. This was because the sensor's sensitivity increased when the prisms were closer to the electrodes.

## V. DISCUSSIONS AND CONCLUSIONS

Here, we developed a six-axis displacement sensor integrated into an RCC device. To measure the six-axis F/T and displacement, capacitance sensing cells were arranged into a structure dedicated to integrating the sensor into the RCC device. The developed sensor comprises only a few parts, and can be assembled only by bolt connections. It is therefore inexpensive and easy to manufacture. As the capacitance measurement unit is built-in, no additional measurement device is required; hence, it is very easy to combine it with devices such as an RCC device. Calibration was conducted considering the geometry of the sensor and device, and experimental data. The sensor's performance was evaluated using different experimental setups. According to the characteristics of the RCC device, the resolution differs in the force and torque values due to high axial rigidity. In future studies, we plan to install the developed RCC device into a manipulator robot. We would then use the said robot to perform various tasks with controllers, using the displacement and force data obtained from the six-axis displacement sensor.

The stiffness of the RCC presented in this article was determined by commercial compliance bars. The RCC used here had a relatively large three-axis displacement ($d_x, d_y, \theta_z$); hence, it could be measured with a much higher resolution than the general force sensors. Conversely, the remaining three axes ($d_z, \theta_x, \theta_y$) had relatively high stiffness; hence, they had low sensitivities due to their small displacements. Nevertheless, it is meaningful to measure the six-axis displacement itself, and a sensor that can simultaneously measure mm-scale six-axis displacement and that can fit in a narrow space inside an RCC will have a wide variety of applications. In addition, in the case of an RCC, if a compliance bar were to be made to have similar vertical and horizontal stiffness values, six-axis force sensing would be able to measure both to a high degree of sensitivity. Furthermore, it would be possible to use the presented device as a six-axis F/T sensor for force control in existing compliance devices, providing they feature mm-scale displacements.

## REFERENCES

[1] R. Usubamatov and K. W. Leong, "Analyses of peg-hole jamming in automatic assembly machines," *Assem. Autom.*, vol. 31, no. 4, pp. 358–362, Sep. 2011.

[2] H. Park, J. Park, D.-H. Lee, J.-H. Park, M.-H. Baeg, and J.-H. Bae, "Compliance-based robotic peg-in-hole assembly strategy without force feedback," *IEEE Trans. Ind. Electron.*, vol. 64, no. 8, pp. 6299–6309, Aug. 2017.

[3] R. K. Jain, S. Majumder, and A. Dutta, "SCARA based peg-in-hole assembly using compliant IPMC micro gripper," *Robot. Auto. Syst.*, vol. 61, no. 3, pp. 297–311, Mar. 2013.

[4] W. Chen, S. Chen, J. Qu, and W. Chen, "A large-range compliant remote center of motion stage with input/output decoupling," *Precis. Eng.*, vol. 51, pp. 468–480, Jan. 2018.

[5] H. S. Choi, Y. G. Lee, M. B. Hong, and Y. J. Choi, "A novel geometric design method of elastic structure for 6-axis force/torque sensor," *IEEE Access*, vol. 7, pp. 166564–166577, 2019.

[6] U. Kim, Y. B. Kim, D.-Y. Seok, J. So, and H. R. Choi, "A surgical palpation probe with 6-axis force/torque sensing capability for minimally invasive surgery," *IEEE Trans. Ind. Electron.*, vol. 65, no. 3, pp. 2755–2765, Mar. 2018.

[7] *Multi-Axis Force/Torque Sensor*, ATI Industrial Automation, Apex, NC, USA, 2013.

[8] J. Ma and A. Song, "Fast estimation of strains for cross-beams six-axis force/torque sensors by mechanical modeling," *Sensors*, vol. 13, no. 5, pp. 6669–6686, May 2013.
[9] B. Wu, J. Luo, F. Shen, Y. Ren, and Z. Wu, "Optimum design method of multi-axis force sensor integrated in humanoid robot foot system," *Measurement*, vol. 44, no. 9, pp. 1651–1660, Nov. 2011.
[10] I. Payo, J. M. Adanez, D. R. Rosa, R. Fernandez, and A. S. Vazquez, "Six-axis column-type force and moment sensor for robotic applications," *IEEE Sensors J.*, vol. 18, no. 17, pp. 6996–7004, Sep. 2018.
[11] M.-Y. Chen, S.-C. Huang, S.-K. Hung, and L.-C. Fu, "Design and implementation of a new six-DOF maglev positioner with a fluid bearing," *IEEE/ASME Trans. Mechatronics*, vol. 16, no. 3, pp. 449–458, Jun. 2011.
[12] Q. Liang, D. Zhang, Q. Song, Y. Ge, H. Cao, and Y. Ge, "Design and fabrication of a six-dimensional wrist force/torque sensor based on E-type membranes compared to cross beams," *Measurement*, vol. 43, no. 10, pp. 1702–1719, Dec. 2010.
[13] L. Fu, A. Song, and D. Chen, "A polyetheretherketone six-axis force/torque sensor," *IEEE Access*, vol. 7, pp. 105391–105401, 2019.
[14] U. Kim, D.-H. Lee, Y. B. Kim, D.-Y. Seok, and H. R. Choi, "A novel 6-axis force/torque sensor for robotic applications," *IEEE/ASME Trans. Mech.*, vol. 22, no. 3, pp. 1381–1391, Jun. 2017.
[15] D.-H. Lee, U. Kim, H. Jung, and H. R. Choi, "A capacitive-type novel six-axis force/torque sensor for robotic applications," *IEEE Sensors J.*, vol. 16, no. 8, pp. 2290–2299, Apr. 2016.
[16] O. Al-Mai, M. Ahmadi, and J. Albert, "Design, development and calibration of a lightweight, compliant six-axis optical force/torque sensor," *IEEE Sensors J.*, vol. 18, no. 17, pp. 7005–7014, Sep. 2018.
[17] N. Hendrich, F. Wasserfall, and J. Zhang, "3D printed low-cost force-torque sensors," *IEEE Access*, vol. 8, pp. 140569–140585, 2020.
[18] *Compensator RCC–Remote Center Compliance Device*, ATI Industrial Automation, Apex, NC, USA, 2012.
[19] U. Kim, D.-H. Lee, W. J. Yoon, B. Hannaford, and H. R. Choi, "Force sensor integrated surgical forceps for minimally invasive robotic surgery," *IEEE Trans. Robot.*, vol. 31, no. 5, pp. 1214–1224, Oct. 2015.
[20] U. Kim, Y. B. Kim, J. So, D. Y. Seok, and H. R. Choi, "Sensorized surgical forceps for robotic-assisted minimally invasive surgery," *IEEE Trans. Ind. Electron.*, vol. 65, no. 12, pp. 9604–9613, Mar. 2018.
[21] U. Kim, H. Jeong, H. Do, J. Park, and C. Park, "Six-axis force/torque fingertip sensor for an anthropomorphic robot hand," *IEEE Robot. Autom. Lett.*, vol. 5, no. 4, pp. 5566–5572, Oct. 2020.

**UIKYUM KIM** (Member, IEEE) received the B.S. and Ph.D. degrees in mechanical engineering from Sungkyunkwan University (SKKU), Suwon, South Korea, in 2011 and 2017, respectively.

Since 2017, he has been a Senior Researcher with the Department of Robotics and Mechatronics, Korea Institute of Machinery and Materials, Daejeon, South Korea. His research interests include robot hand, surgical robot, six-axis force/torque sensor, force/tactile sensors for robotics applications, haptic interfaces, force-feedback control system, dexterous manipulators for industrial robotics, soft sensor, and sensor calibration computing algorithms.

**DONG IL PARK** received the B.S. and M.S. degrees in mechanical engineering and the Ph.D. degree from the Korea Advanced Institute of Science and Technology in 2000, 2002, and 2006, respectively. Since 2006, he has been with the Korea Institute of Machinery and Materials, where he has been involved in robotics. His research interests include design, control, and application of robot manipulators and mobile robots.

**GWANGHYUN JO** received the B.S., M.S., and Ph.D. degrees from the Department of Mathematical Sciences, KAIST, Daejeon, South Korea, in 2018. From 2018 to August 2019, he was a Postdoctoral Researcher with KAIST. He has been on the faculty with the Department of Mathematics, Kunsan National University, since 2019. His research interests include numerical analysis and simulation of various fluids problems arising from hemodynamics, petroleum engineering.

**HEEYEON JEONG** received the B.S. degree in mechanical engineering from Sungkyunkwan University, Suwon, South Korea, in 2019, where he is currently pursuing the M.S. degree with the Department of Artificial Intelligence and Robotics.

Since 2019, he has been a Researcher with the Department of Robotics and Mechatronics, Korea Institute of Machinery and Materials, Daejeon, South Korea. His research interests include multi-axis force/torque sensor, sensor calibration, and kinematic analysis.

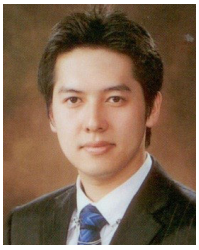

**HWI-SU KIM** received the B.S. and Ph.D. degrees in mechanical engineering from Korea University, in 2007 and 2014, respectively. He was with the School of Mechanical Engineering, Korea University. He is currently a Senior Researcher with the Korea Institute of Machinery and Materials. His research interests include manipulator design, counterbalance mechanism, and safe robot arms.

**SUNG-HYUK SONG** received the B.S. degree in physics from Korea University, Seoul, South Korea, in 2011, and the Ph.D. degree in mechanical engineering from Seoul National University, Seoul, in 2017.

Since 2017, he has been a Senior Researcher with the Department of Robotics and Mechatronics, Korea Institute of Machinery and Materials, Daejeon, South Korea. His research interests include soft robotics, universal soft gripper, soft actuator, application using smart structure, smart composite actuator, SMA-based robot, biomimetic robot, morphing wheel mechanism, soft wearable robot, stiffness-variable structure, and shape-adaptive structure.

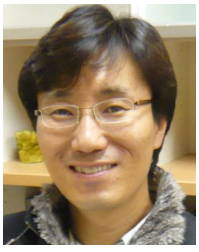

**CHANHUN PARK** received the B.S. degree in mechanical engineering from Yeungnam University, in 1994, the M.S. degree from POSTECH, in 1996, and the Ph.D. degree from KAIST, South Korea, in 2010.

Since 1996, he has been a Principal Researcher with the Department of Robotics and Mechatronics, Korea Institute of Machinery and Materials, Daejeon, South Korea. His research interests include dual arm robot, high-speed parallel robot, cooperative robot, force-feedback control system, dexterous manipulators for industrial robotics, human–robot cooperation, and robotic wheelchair.